

## MIT Open Access Articles

*Perfectly phase-matched third-order distributed feedback terahertz quantum-cascade lasers*

The MIT Faculty has made this article openly available. **Please share** how this access benefits you. Your story matters.

**Citation:** Kao, Tsung-Yu, Qing Hu, and John L. Reno. "Perfectly Phase-Matched Third-Order Distributed Feedback Terahertz Quantum-Cascade Lasers." *Optics Letters* 37, no. 11 (June 1, 2012): 2070. © 2012 Optical Society of America

**As Published:** <http://dx.doi.org/10.1364/OL.37.002070>

**Publisher:** Optical Society of America

**Persistent URL:** <http://hdl.handle.net/1721.1/86373>

**Version:** Final published version: final published article, as it appeared in a journal, conference proceedings, or other formally published context

**Terms of Use:** Article is made available in accordance with the publisher's policy and may be subject to US copyright law. Please refer to the publisher's site for terms of use.



# Perfectly phase-matched third-order distributed feedback terahertz quantum-cascade lasers

Tsung-Yu Kao,<sup>1,\*</sup> Qing Hu,<sup>1</sup> and John L. Reno<sup>2</sup>

<sup>1</sup>Department of Electrical Engineering and Computer Science & Research Laboratory of Electronics, Massachusetts Institute of Technology, Cambridge, Massachusetts 02139, USA

<sup>2</sup>Center for Integrated Nanotechnology, Sandia National Laboratories, MS 1303, Albuquerque, New Mexico 87185, USA

\*Corresponding author: wilt\_kao@mit.edu

Received January 19, 2012; revised March 30, 2012; accepted April 2, 2012;  
posted April 2, 2012 (Doc. ID 161825); published May 30, 2012

We report a novel laser cavity design in third-order distributed feedback (DFB) terahertz quantum-cascade lasers based on a perfectly phase-matching technique. This approach substantially increases the usable length of the third-order DFB laser and leads to narrow beam patterns. Single frequency emissions from 151 apertures (5.6 mm long device) are coherently added up to form a narrow beam with (FWHM  $\approx 6 \times 11^\circ$ ) divergence. A similar device with 40 apertures shows more than 5 mW of optical power with slope efficiency  $\sim 140$  mW/A at 10 K pulsed operation. © 2012 Optical Society of America

OCIS codes: 140.3070, 140.0140.

Terahertz quantum-cascade lasers (QCLs) are expected to find applications in the near future as local oscillators for submillimeter wave heterodyne receiver systems at frequencies above 1 THz [1]. Their low power consumption and small form factors make them suitable for applications in astrophysics and remote sensing. A robust single-mode laser that can sustain continuous-wave (cw) operation and emit  $>1$  mW of optical power in a narrow and symmetric beam pattern is highly desired in these applications.

The best terahertz QCLs in terms of high-temperature operation have been demonstrated based on the metal-metal (MM) waveguides [2], which provide strong mode confinement and low waveguide losses. However, because of the subwavelength confinement of the waveguide, the far-field beam pattern of a Fabry–Perot (F-P) MM THz laser is far from ideal Gaussian beams [3]. Several approaches [4] have been demonstrated to address this issue, such as photonic crystals [5] or surface-emitting distributed feedback (DFB) laser arrays [6,7]. The majority of these approaches focus on enlarging the two-dimensional light-emitting area and thus suffer from degradation in cw performance because of their large power dissipation and difficulty in heat removal. Recently, an ingenious solution based on third-order DFB structures [8,9] utilizes the so-called end-fire antenna effect to achieve tight beam patterns with minimum negative impact on cw performance.

The effectiveness of the end-fire antenna depends on the phase-matching condition between the free-space propagating radiation and the electric field inside each emission aperture. Figure 1(c) shows the electric field inside a third-order DFB laser. One can model these adjacent apertures as point radiation sources with opposite polarities. If the modal index  $n_{\text{eff}}$  is close to 3 in the waveguide, the distance between two adjacent apertures for third-order DFB gratings will be roughly half of the free-space wavelength  $\lambda_0$ . It is clear that the radiation from each opening will constructively add up at two far ends of this one-dimensional end-fire antenna array.

One can define an effective index as  $n_{\text{eff}} = 3 \times \lambda_0 / (2 \times \Lambda)$ , where  $\lambda_0$  is the free-space wavelength and  $\Lambda$  is the distance between adjacent apertures (the grating

period).  $n_{\text{eff}}$  can be treated as a figure-of-merit for evaluating the phase-matching condition. When  $n_{\text{eff}} = 3$ , since the electric field between adjacent apertures has  $180^\circ$  phase difference for the third-order grating, the phase-matching condition is perfectly met; but for  $n_{\text{eff}} \neq 3$ , phase errors will accumulate along the array. Emissions from different parts of the array then destructively cancel out after a certain device length. Figures 1(a) and 1(b) show the beam patterns of third-order DFB lasers with different grating periods. While emissions constructively add up and create narrower beam patterns for a longer device under the perfectly phase-matching condition, destructive superposition clearly happens under the mismatched condition. Similar to the coherence length concept in the nonlinear optical generation of radiations, we can define a coherence length  $L_c$  as the length over which the relative phase of two collinearly traveling waves changes by  $\pi$ . Using the definition of  $n_{\text{eff}}$ , we have  $L_c = \Lambda \times n_{\text{eff}} / |n_{\text{eff}} - 3|$ . For  $n_{\text{eff}} \approx 3.2$ , this coherence length would be  $\sim 16\Lambda$ , beyond which the beam pattern begins to degrade and the output power will

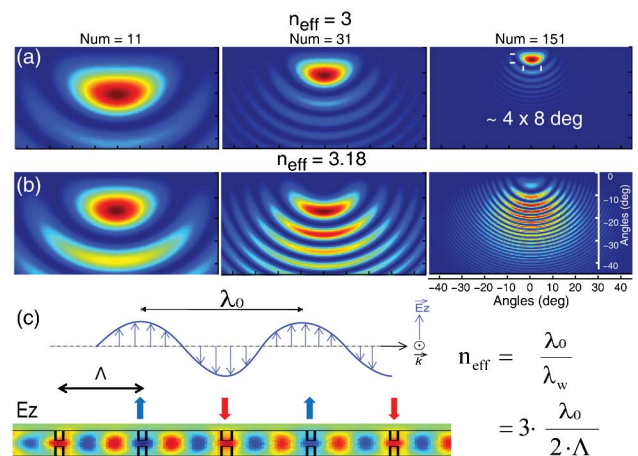


Fig. 1. (Color online) Simulated beam patterns of different third-order DFB lasers using similar method in [9], (a) under perfectly phase-matched condition  $n_{\text{eff}} = 3$ , (b) at  $n_{\text{eff}} = 3.18$ , (c) with the electric field inside a corrugated third-order DFB laser and the schematic for the free-space propagating radiation.

actually *decrease*. Because of the high refractive index ( $n \approx 3.6$ ) in GaAs, even though trench structures have been adopted to reduce  $n_{\text{eff}}$ , it is still far from three (3.2–3.4 from [8,9]) and thus restricts the maximum usable length of the third-order DFB lasers.

In this letter, we present the implementation of a novel geometry that will introduce another degree of freedom to adjust the effective index to achieve the perfectly phase-matching condition. It substantially increases the usable length of third-order DFB lasers and leads to narrower beam patterns. Figure 2(f) shows the schematic of a perfectly matched (PM) laser, which consists of short laser cavities (A) and contact fins (B). The lasing frequency is mainly determined by dimensions of each cavity and is a weak function of the gap distance between cavities. The gap size can then be chosen to meet the phase-matching condition. One can regard these cavities as identical F-P lasers that phase lock to each other, forming a one-dimensional phased array. When the phase-matching condition is met, the spacing between adjacent gaps ( $\lambda_o/2$ ) will also satisfy the resonance condition described in a leaky-wave coupled scheme. As pointed out in [10], such a leaky-wave coupled structure near its resonance condition is equivalent to the standard perturbation coupled-mode DFB lasers. Thus, even though the index contrast between gain medium and air gap is high, because of almost 100% transmission,

the resonant leaky-wave coupled cavities form a third-order DFB structure.

Figure 2(c) shows the simulated envelope functions of the normalized field energy density from two DFB lasers with the same cavity length but different gap sizes. The dimensions were chosen so that one will meet the perfectly phase-matching condition ( $n_{\text{eff}} = 3$ ). The gap size for the other laser is smaller, yielding  $n_{\text{eff}} > 3$ . Although laser cavities are closer to each other under the non-PM condition, the field energy distribution is still more “localized” in the center (decaying faster from center to edge). Figure 2(d) shows a close view of energy density distribution near the edge of the array. While cavities near the edge under the non-PM condition have negligible energy density, they still maintain 10%–20% of the peak energy density when the PM condition is met. This can be explained by the fact that when  $n_{\text{eff}}$  is close to 3, the array geometry also satisfies the resonance condition previously mentioned, and thus long-range coupling beyond adjacent cavities is possible.

The biasing current is provided to the laser through the contact pins that connect to the bonding pad. The position of the contact pin is chosen to minimize the disturbance to the desired modes in laser cavities. Finite-element method (FEM) simulation shows no significant increase in metal loss from introducing the contact pins. A thin  $\text{SiO}_2$  layer was deposited between the bonding pad and gain medium to ensure electrical isolation. It should be pointed out that while the perfectly phase-matching condition can also be met in corrugated third-order DFB lasers [such as the one illustrated in Fig. 2(e)] by shrinking the laser ridge width, it would require  $\sim 10 \mu\text{m}$  ridge width for a laser operating at 3 THz to meet the perfectly matched condition. Such a narrow width will reduce the mode confinement factor and cause an undesired increase in the lasing threshold. Furthermore, PM cavities also enable a biasing individual cavity through separate pins, reducing the current density flowing on top of the metal, which is essential for longer arrays.

The THz QCL gain medium, labeled as FL183S, grown by molecular-beam epitaxy (wafer VB0112) was first Cu-Cu thermal bonded with an  $n^+$  GaAs receptor wafer, annealed, and substrate-removed to expose the  $10 \mu\text{m}$  thick QCL structure. A  $300 \text{ nm}$  thick  $\text{SiO}_2$  was blanket deposited as the electric isolation layer using plasma-enhanced chemical vapor deposition (PECVD), followed by an oxide etch to open the top of laser cavities. The top metal of laser cavities along with the contact fins and the bonding pads were defined using image reversal photoresist AZ-5214 and a lift-off process (Ti/Au,  $15/390 \text{ nm}$ ). The top metal patterns then were used as the self-aligned masks in electron cyclotron resonance reactive ion etching (ECR-RIE) to form the laser cavities. The wafer was further lapped down, and then bottom electric contact (Ti/Au  $15/250 \text{ nm}$ ) was deposited. The devices were then die sawed into smaller subchips, indium die bonded to a copper chip carrier, wire bonded, and then mounted to a pulsed tube cryorefrigerator or a helium cryostat, where the  $L-I-V$  curves of the devices were measured at a temperature of 10 K in pulse mode using a He-cooled Ge:Ga photodetector (at 4 K using a pyroelectric detector for cw measurement).

Figure 3(a) shows measured  $J-V$  curve and  $L-J$  curve for two PM laser devices with different lengths.

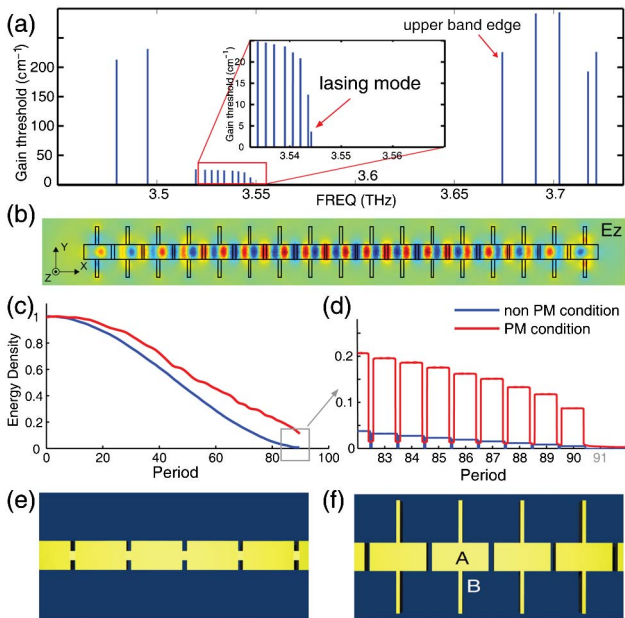


Fig. 2. (Color online) (a) Computed radiation losses versus eigenfrequencies based on three-dimensional FEM simulations of PM third-order DFB lasers. (b) Electric fields of the lasing mode inside a 17-period PM laser. Lasing wavelength  $\lambda_o$  is  $84.6 \mu\text{m}$  with  $42.3 \mu\text{m}$  periodicity results  $n_{\text{eff}} = 3$ . (c) Envelopes of normalized energy density inside a 181-period DFB laser under PM condition and non-PM ( $n_{\text{eff}} = 3.4$ ) condition. Only half of the laser is shown. The envelope under the PM condition decays slower than its non-PM counterpart. Zoom in to show the detailed density distribution near the end in (d). Each plateau of the squarelike curve represents one period of the laser cavity, and the valley represents the gap between two adjacent cavities. (e) Valley view schematic for a corrugated third-order DFB laser, and (f) a PM third-order DFB laser. The laser cavity and the contact fin are labeled as A and B.

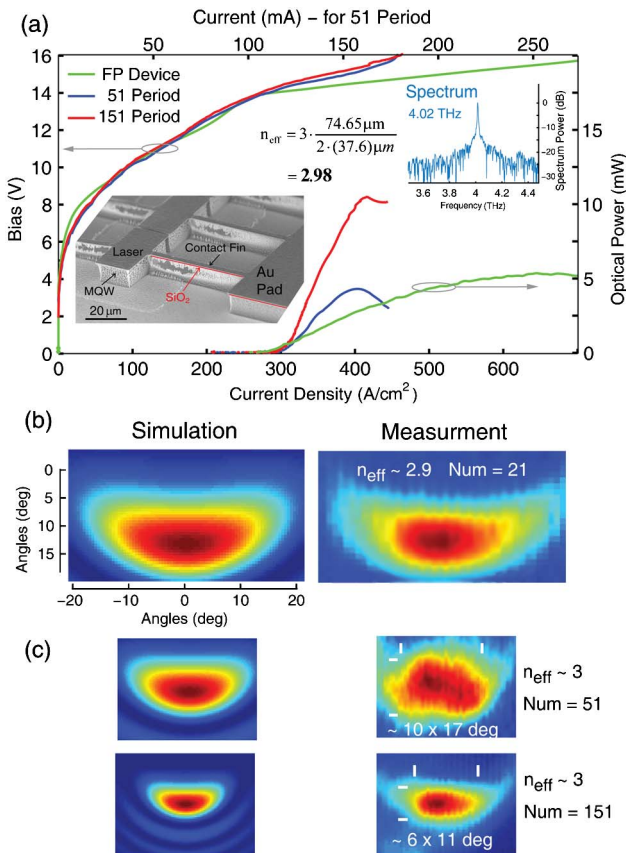


Fig. 3. (Color online) (a) Measured cw  $L$ - $J$ - $V$  curves and beam patterns from a 51-period laser, a 151-period PM laser, and a  $40 \times 1.34$  mm F-P laser (cleaved facet with Winston cone). The dimensions of each cavity are  $22 \times 34.8 \mu\text{m}$  with  $\sim 2.8 \mu\text{m}$  gap [see inset ( $\sim 1.9$  mm long for the 51-period laser)], with lasing frequency at 4.02 THz (pulsed) yielding  $n_{\text{eff}} \sim 2.98$ . Both 51- and 151-period lasers show single-mode operation at all biases. (b) Comparison between simulation and measured beam pattern for a  $n_{\text{eff}} \sim 2.90$  device. (c) Same comparison for two PM third-order DFB lasers ( $n_{\text{eff}} \sim 2.98$ ) with different lengths. Beam patterns were measured with a pyroelectric detector on a two-dimensional rotating stage at  $\sim 20$  cm distance.

The  $J$ - $V$  curves from two devices match quite well, indicating the uniformity of devices and bias conditions. The threshold current density  $J_{\text{th}}$  is  $290 \text{ A/cm}^2$  with peak optical power output at  $410 \text{ A/cm}^2$ . The maximum lasing temperature ( $T_{\text{max}}$ ) is 110 K (pulsed) and 80 K (cw). The beam divergences for the 51-period and the 151-period devices are  $\sim 10 \times 17^\circ$  and  $6 \times 11^\circ$ , respectively [Fig. 3(c), right]. While the divergence in the solid angle is roughly inverse proportional to the length of the devices, the output power also increases by  $\sim 2.6\times$  from 5 to  $\sim 13$  mW (10% duty-cycle), and 4.5 to  $\sim 11$  mW (cw). A  $40 \mu\text{m}$  wide dry-etched F-P laser with comparable length on the same gain medium has 5.3 mW cw power,  $T_{\text{max}} \sim 150$  K (pulsed), and 101 K (cw). A clear increase in slope efficiency from the F-P laser to PM lasers is observed. Devices with  $n_{\text{eff}} < 3$  were also tested for comparison. Figure 3(b) shows the pulsed beam pattern for a  $n_{\text{eff}} \sim 2.90$  device. Simulated and measured data show excellent agreement for devices with different lengths and effective indices. Another 41-period (1.6 mm long) PM laser ( $n_{\text{eff}} = 2.99$ ) lasing at

$\sim 3.83$  THz emits  $\sim 5.1$  mW of pulsed power at 10 K with beam-pattern divergence  $\sim 11 \times 15^\circ$  (data not shown) and slope efficiency  $\sim 140 \text{ mW/A}$ . Although we successfully achieved perfect phase matching in our devices, we see no significant improvement in performance compared to the devices reported in [9]. We attributed this to the porous and concave cavity sidewall from our current dry-etch process (clearly shown in the scanning electron microscope pictures in Fig. 3(a)). The porous sidewall increases waveguide losses, reducing the slope efficiency and power, while the concave sidewall decreases bias uniformity and impacts dynamic range.

The PM concept could easily be applied to other frequencies, but because of the delicate nature of the phase-matching condition, more than 20 design variations with  $\sim 0.3 \mu\text{m}$  increment in gap size are required to achieve perfectly phase-matching within  $< 1\%$  error. Restricted by our limited fabrication area, we can only demonstrate the PM technique at one specific frequency in this work.

In summary, we have demonstrated a novel cavity design for third-order DFB THz QCLs. An array of identical cavities are carefully spaced to ensure the free-space laser radiation excited by the structure and the electric field at each aperture meet the phase-matching condition. Up to 151 laser sectors are phase locked to form a single-lobe beam pattern with full-width half maximum  $\approx 6 \times 11^\circ$  at end-fire direction. This approach substantially increases the usable length of a third-order DFB laser while keeping a high slope efficiency.

This work is supported by NASA and NSF, and also performed, in part, at the Center for Integrated Nanotechnologies, a U.S. Department of Energy, Office of Basic Energy Sciences user facility. Sandia National Laboratories is a multiprogram laboratory managed and operated by Sandia Corporation, a wholly owned subsidiary of Lockheed Martin Corporation, for the U.S. Department of Energy's National Nuclear Security Administration under contract DE-AC04-94AL85000.

## References

1. J. R. Gao, J. N. Hovenier, Z. Q. Yang, J. J. A. Baselmans, A. Baryshev, M. Hajenius, T. M. Klapwijk, A. J. L. Adam, T. O. Klaassen, B. S. Williams, S. Kumar, Q. Hu, and J. L. Reno, *Appl. Phys. Lett.* **86**, 244104 (2005).
2. B. S. Williams, S. Kumar, H. Callebaut, Q. Hu, and J. L. Reno, *Appl. Phys. Lett.* **83**, 2124 (2003).
3. A. J. L. Adam, I. Kašalynas, J. N. Hovenier, T. O. Klaassen, J. R. Gao, E. E. Orlova, B. S. Williams, S. Kumar, Q. Hu, and J. L. Reno, *Appl. Phys. Lett.* **88**, 151105 (2006).
4. L. Mahler and A. Tredicucci, *Laser Photon. Rev.* **5**, 647 (2011).
5. Y. Chassagneux, R. Colombelli, W. Maineult, S. Barbieri, H. E. Beere, D. A. Ritchie, S. P. Khanna, E. H. Linfield, and A. G. Davies, *Nature* **457**, 174 (2009).
6. S. Kumar, B. S. Williams, Q. Qin, A. W. M. Lee, Q. Hu, and J. L. Reno, *Opt. Express* **15**, 113 (2007).
7. T.-Y. Kao, Q. Hu, and J. L. Reno, *Appl. Phys. Lett.* **96**, 101106 (2010).
8. M. I. Amanti, M. Fischer, G. Scalari, M. Beck, and J. Faist, *Nat. Photon.* **3**, 586 (2009).
9. M. I. Amanti, G. Scalari, F. Castellano, M. Beck, and J. Faist, *Opt. Express* **18**, 6390 (2010).
10. D. V. Vysotskii and A. P. Napartovich, *J. Exp. Theor. Phys.* **88**, 227 (1999).